ACS APPLIED NANO MATERIALS

www.acsanm.org Article

Sustainable Manufacturing of Vertical Carbon Nanotube (CNT) Arrays Inside Insulating Nanoporous Membranes Using Nickel Magnetic Nanowires (MNWs)

Roman Kolisnyk,* Morgen L. Smith, Nicholas C. A. Seaton, Michael L. Odlyzko, Olha Masiuchok, Jeanne Riga, Placidus B. Amama, and Bethanie J. H. Stadler*

Cite This: *ACS Appl. Nano Mater.* 2024, 7, 24866−24874 Read Online

ACCESS | Metrics & More | Article Recommendations | Supporting Information

ABSTRACT: Carbon nanotubes (CNTs) were successfully synthesized using industrial waste gases by chemical vapor deposition inside vertically oriented nanopores of insulating membranes. Importantly, the waste products from Fischer−Tropsch synthesis were used as the carbon source rather than typical purified sources, and this recycling of carbon is important for the sustainability of our environment. Specifically in this work, vertical CNT arrays were achieved using nickel (Ni) magnetic nanowires (MNWs) catalysts that were prepared by template electrochemical deposition inside 50 μm-thick nanoporous anodized aluminum oxide (AAO). Here, the nanopore diameter (20−200 nm) and Ni MNW length (45 and 25 μm) were varied to study the impact on CNT growth characteristics. Raman spectroscopy, scanning electron microscopy, transmission electron microscopy, and field emission spectroscopy were used to characterize CNTs on Ni MNWs. For long MNWs (45 μm), the Ni catalyst was just below the AAO surface, so CNT diameters did not change appreciably with the MNW diameter. Alternatively, for short MNWs (25 μm), the carbon source gases had to diffuse into the AAO nanopores before reacting with the Ni catalyst, and both the CNT diameter and yield increased with the nanopore diameter. Highly crystalline CNTs were formed from particles of Ni catalyst, although for smaller diameter nanopores, the Ni catalyst particle could be blocked by template pore wall defects, resulting in subsequent amorphous nanofiber growth above the blocked particle. Optimally, CNT synthesis was observed for 25 μm MNWs grown in 80 nm AAO nanopores, maximizing field emission current at 480 μA/cm^2 (at electric field 0.5 V/μm) with a turn-on field of 0.26 V/μm.

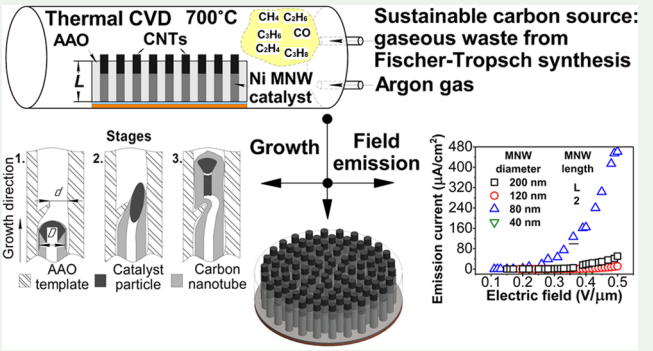

KEYWORDS: *carbon nanotube arrays, porous anodic aluminum oxide, magnetic nanowires, sustainable CNT growth, field emission*

1. INTRODUCTION

Carbon nanotubes (CNTs) are desired in various technological applications due to their remarkable intrinsic properties: high mechanical strength, outstanding thermal and electrical conductivity, and chemical stability.[1] All of these make CNTs potential candidates for nanoscale applications as capacitors,[2] field emitters,[3−6] sensors[7−9] and other related devices.[10−12]

The most scalable and controllable growth of CNTs is catalytic or noncatalytic chemical vapor deposition (CVD).[13] Synthesis of CNTs via the CVD process requires strict control of conditions in terms of catalyst properties, temperature, and feedstock type and composition.[13] The growth typically occurs on a transition metal (Co, Fe, or Ni) catalyst[14] supported by a refractory oxide (such as SiO_2 or Al_2O_3) and utilizes purified, expensive hydrocarbon gases as feedstocks. Additionally, commonly used feedstocks, such as ethylene and acetylene, are produced via technologies that are not environmentally sustainable, and their use in CVD growth requires tight process control and extensive optimization. Therefore, efforts to achieve widespread applications of CNTs will benefit significantly from the development of scalable, sustainable, and controllable growth processes.

An important application of CNTs is field emission.[3−6,15−18] Effective field emitters must possess a low turn-on field, high emission current density, long emission stability, and high field enhancement factor.[19] These parameters are mainly controlled by the emitter aspect ratio, density, and structure. CNTs satisfy all of the above and offer high emission currents at low electric fields in comparison to other field emitters.[19] Unlike CNTs,

Received: August 19, 2024
Revised: October 7, 2024
Accepted: October 11, 2024
Published: October 18, 2024

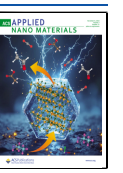

graphene and graphene-based materials are planar emitters, which only show acceptable field emission properties with vertical alignment.[20]

The first successful field emission testing of CNTs[21,22] is credited to their high aspect ratio, excellent electrical properties, and strong carbon−carbon bonding.[21,23] Since then, CNTs have been subjected to deep fundamental and technological investigations.[13,20] Multiwalled CNTs withstand ion bombardment and irradiation during emission more effectively than single-walled CNTs.[20] When CNTs are grown on catalytic metals, good electrical and thermal contact at the catalyst-nanotube interface facilitates electron transport and heat dissipation from the cathode, respectively.[24,25]

Gate-type CNT cathodes have been of particular interest for new space applications, such as electric propulsion,[3] where deep-space missions require uniform electron emissions that can be best obtained by gated electrodes. Hung[26] and Nilsson[27] showed that some gates can even self-bias, but screening can still be a problem.

This paper revisits a fabrication method previously employed for flat screen displays, namely CNT growth in anodic aluminum oxide (AAO) with a catalyst, here Ni magnetic nanowires (MNWs).[28−30] MNWs have been popular recently for applications as nanobarcodes,[31] which were decoded using first-order reversal curves,[32] and for many bioapplications[33] as ferromagnetic alternatives to superparamagnetic iron oxide nanoparticles.[34,35] Although MNWs are not commonly used as substrates, their size facilitates the easy nanoparticle formation on the surface before growing CNTs.[36−39]

Here, we demonstrate for the first time the use of industrial gaseous waste from the Fischer−Tropsch synthesis (FTS) process for CVD growth of CNT arrays from MNWs embedded in an AAO. The growth of CNTs employing these nontraditional substrates and geometries is enhanced by the unique properties of the feedstock. The growth process, along with the use of an earth-abundant metal as a catalyst, will enhance the long-term sustainability of CNT manufacturing and provide a viable pathway for the scalable and controllable growth of CNTs. Given the high proportion of methane (30 vol %) in the industrial waste used as a feedstock, the study will also benefit research efforts aimed at improving the utilization of natural gas. Many countries, including the United States, are well positioned to benefit from any technology that can utilize the enormous reserves of shale gas resources, including the growth of vertically oriented CNTs presented here. In addition, this study elucidates the influence of the MNW diameter (40−200 nm) and length (45 and 25 μm) on CNT growth behavior. Whereas the pore spacing of the AAO template can be precisely controlled, the emitters can be grown at the closest possible spacing before shielding from adjacent emitters becomes problematic, which allows for fine-tuning for optimal field emission. When also considering the environmental sustainability and reduced manufacturing cost associated with using industrial waste products as feedstock, this well-controlled CNT growth process is highly promising.

2. EXPERIMENTAL SECTION

2.1. Fabrication of Ni Magnetic Nanowires in AAO. The preparation of Ni MNWs was conducted by templated electrochemical deposition using AAO membranes (13 mm diameter, 50 μm thickness) with various nanopore diameters (20, 40, 120, and 200 nm) from InRedox. One side of the AAO template was sputtered with a 7 nm adhesive layer of titanium, followed by a 500 nm layer of copper as a working electrode. A nickel mesh was used as the counter electrode, and Ag/AgCl was used as the reference electrode from which all of the reduction potentials below are referred. Ni MNWs were deposited from an aqueous electrolyte of 0.5 M H_3BO_3, 1 M $NiSO_4{\cdot}(H_2O)_6$ with pH 3 at 20 °C using a potentiostat (Gamry Instrument) with a pulsed potential (−0.85/−0.95 V). An initial 10 min treatment using a lower pulsed voltage (−0.8/−0.85 V) was used first to initiate a slow ion transport rate at the beginning of electrodeposition to nucleate MNW growth in the nanopores. The AAO templates were attached to a rotating disk electrode (Gamry) to linearize the diffusion boundary layer near the cathode, which enhances the uniformity and slows the deposition rate to ∼3.3 nm/s. A slow deposition rate enables the MNW length to be accurately controlled by varying the total electroplating time. After Ni growth, the samples were cleaned with deionized water and ethanol in an ultrasonic cleaner. For the four AAO nanopore diameters, MNWs were grown to two lengths: full (∼45 μm) and half (∼25 μm) AAO thickness.

2.2. Synthesis of CNT Arrays from Ni Nanowires Embedded in AAO. CNT growth was conducted by means of a unique CVD process that utilizes industrial waste products from FTS, as the feedstock. The gaseous waste from the FTS process (FTS-GP) was supplied by Matheson Inc. with the following composition: H_2 (40%), CH_4 (30%), C_2H_6 (8%), C_2H_4 (6%), CO (5%), C_3H_8 (5%), N_2 (4%), and C_3H_6 (2%). The Ni MNWs embedded in the AAO template described in Section 2.1 served as catalysts to nucleate CNT growth after thermal annealing and prereduction steps. Growth was carried out at atmospheric pressure using the EasyTube 101 CVD system (CVD Equipment Corporation), equipped with several essential features to facilitate the repeatability of the growth process, including a LabView-based process control software, a control system for precise temperature control, and a static mixer for optimum gas mixing. A typical growth run involved heating the AAO/Ni substrate to 700 °C at a rate of 45 °C/min in the Ar atmosphere. At 700 °C, the substrate was exposed to an excess amount of H_2 in combination with Ar for 2 min to reduce the catalyst; the respective flow rates were 250 standard cubic centimeters per minute (sccm) of H_2 and 250 sccm of Ar. Thereafter, CNT growth was initiated by introducing a growth gas mixture of 25 sccm FTS-GP and 250 sccm Ar for 15 min. After the growth run ended, the samples were rapidly cooled in H_2, followed by gradual cooling to room temperature in an Ar flow (700 sccm). A schematic roadmap that reflects the steps described in Sections 2.1 and 2.2 is shown in Figure S1.

2.3. Characterization. AAO, MNWs, and CNTs were studied by X-ray diffraction (BRUKER D8 DISCOVER, Co Kα radiation), Raman spectroscopy, and scanning electron microscopy (SEM; JEOL 6500F 0.5−30 keV, Thermo Apreo 2S Lo-Vac 0.2−30 keV), and transmission electron microscopy (TEM; Thermo Talos F200X 200 keV, Thermo Talos F200C 200 keV). Raman spectra of the CNTs were acquired at multiple spots from each sample using a Renishaw Invia Raman Microscope, equipped with a 532 nm laser as the excitation source (1% laser power, 15 acquisitions, 3-s exposure). The measurements were then normalized and averaged, and peaks were fitted with the Lorenz function. I_D/I_G ratio was calculated as the mean value of ratios for all measured spectra of the sample. The standard deviation (SD) of I_D/I_G is shown in Figure 4. For SEM measurements, the studied surface was sputtered with a 5 nm layer of conductive material (Au or Pt). For TEM imaging of CNTs, AAO templates were dissolved in 1 M NaOH, then MNWs with CNTs cleaned and drop casted onto a TEM copper grid. Figure 1 shows a cross-sectional drawing of the experimental apparatus for emission testing of small (<1 cm^2) samples at low powers, withstanding high temperatures without distortion. The chamber was evacuated to a pressure of 100 mTorr and then to ∼6×10^{-6} using mechanical and turbomolecular pumps (Agilent Technologies), respectively. The anode support structure consists of two coaxial, threaded cylinders. The outer cylinder is rigidly mounted to the vacuum chamber, while the inner cylinder can be rotated to adjust the height of the anode above the cathode. The emission current from the cathode was

https://doi.org/10.1021/acsanm.4c04782
ACS Appl. Nano Mater. 2024, 7, 24866−24874

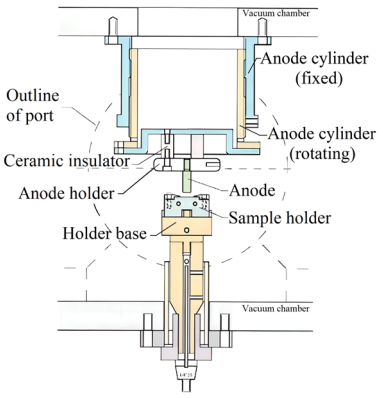

Figure 1. Schematic illustration of the emission testing apparatus.

measured using a picoammeter (Keithley 6485) with a detection limit of 0.01 pA. Stray emission was minimized by using ceramic insulators between the rotating anode cylinder and the anode holder. The input voltage was applied using a 5 kV power source (Keithley 2290-5). The anode is a 1/4 inch diameter molybdenum cylinder with rounded edges positioned 1 cm above the cathode samples. Sample holders were custom machined from 304SS to mount 1 cm diameter samples and slide into a holder base centered under the anode in the vacuum chamber, where it makes metal-to-metal contact with the base. As the anode diameter and thus area are smaller than those of the cathode samples, the anode dimensions define the effective emission area, which is 0.3167 cm^2.

3. RESULTS AND DISCUSSION

First, AAO templates were annealed at different temperatures to determine their limits for the high-temperature CVD growth of CNTs. Figure 2 shows that AAO annealed over 850 °C

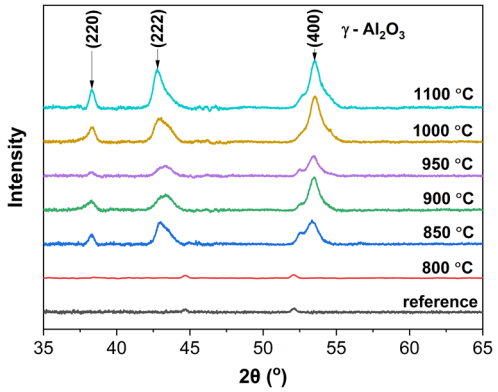

Figure 2. X-ray diffractograms of the annealed AAO templates.

experiences a structural transformation to polycrystalline γ-Al_2O_3. This transformation led to brittle behavior, and the templates were deformed. Moreover, templates with small MNW diameters (20 nm) were very brittle after the high-temperature CVD process.

Figure 3 shows typical fracture surfaces of AAO templates after the growth of Ni MNWs. The MNWs were deposited uniformly in the nanopores. There are pores where MNWs are deformed or missing due to breaking off during template fracture. The AAO templates were 50 μm thick, so the "full" AAO MNW length was chosen to be just below the AAO surface (Figure 3a) to ensure that Ni outgrowths (often called mushrooms[40]) did not form because that would lead to uncontrolled catalyst diameters for the subsequent CNT growth. The half-filled nanopores had 25 μm long MNWs inside (Figure 3b), with the remaining 25 μm of AAO thickness presenting empty nanopores above the MNW catalysts to encourage vertical CNT growth. The AAO pore density is in the range of 10^9–10^{10} cm^{-2} and is shown in Table 1.

Table 1. Pore Density and Porosity of the Templates Used in This Study

pore diameter (nm)	pore density (cm^{-2})	porosity (%)
200 ± 24	5×10^8	16 ± 3
120 ± 14	1.5×10^9	16 ± 2
80 ± 10	3×10^9	15 ± 2
40 ± 4	1×10^{10}	12 ± 2
20 ± 3	5×10^{10}	12 ± 2

Raman spectroscopy is routinely used to evaluate the structural quality of the graphitic lattice in CNTs.[34] Representative Raman spectra of the CNTs grown on Ni MNWs with different aspect ratios are shown in Figure 4a,b. The presence of D- and G-bands indicates that these are multiwalled CNTs.[41] The G-band between 1580 and 1600 cm^{-1} is assigned to the in-plane vibrational of sp^2 carbon–carbon bond in the CNTs, and the D-band at ∼1340 cm^{-1} represents the number of defects, including vacancies, nonuniformity, corrugation, and twisting in the CNTs.[41] The D′ peak located in the vicinity of ∼1615 cm^{-1} is associated with microcrystalline graphite, a byproduct frequently observed in carbon nanomaterials.[42] CNT G-band shifts to wavenumbers above the graphite peak (ω_g = 1582 cm^{-1}) are associated with CNTs curvature[43] and the presence of nanocrystalline graphite,[44] whereas amorphous carbon broadens the peak and shifts it to lower wavenumber.[44] The intensity

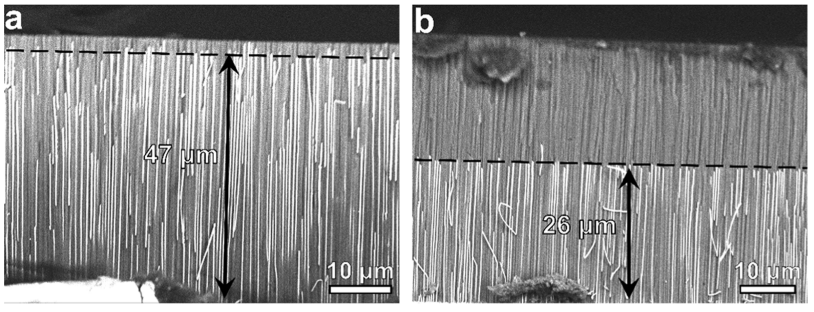

Figure 3. SEM backscattering images of AAO fracture surfaces showing Ni MNWs (bright vertical lines) with nanopore diameters/nanowires lengths of (a) 200 nm/45 μm and (b) 200 nm/25 μm.

https://doi.org/10.1021/acsanm.4c04782
ACS Appl. Nano Mater. 2024, 7, 24866–24874

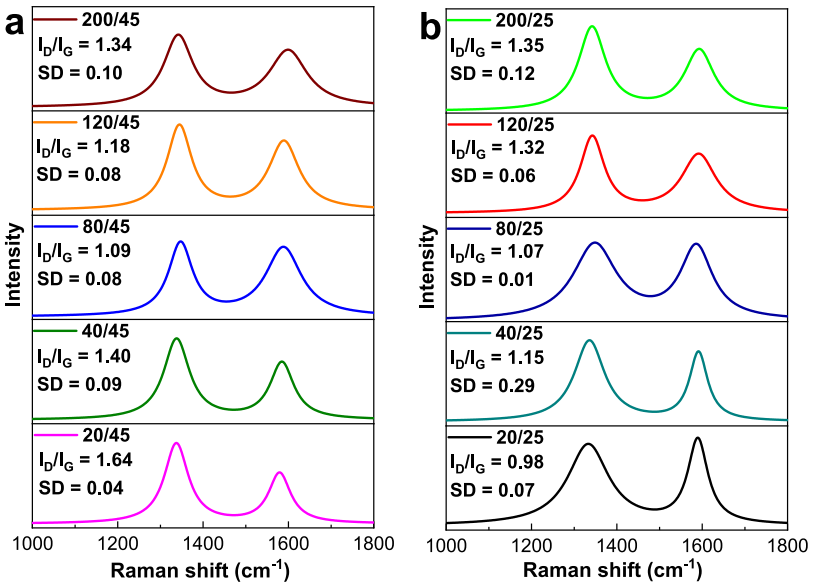

Figure 4. Raman spectra for the CNTs grown on (a) 45 and (b) 25 μm Ni MNWs.

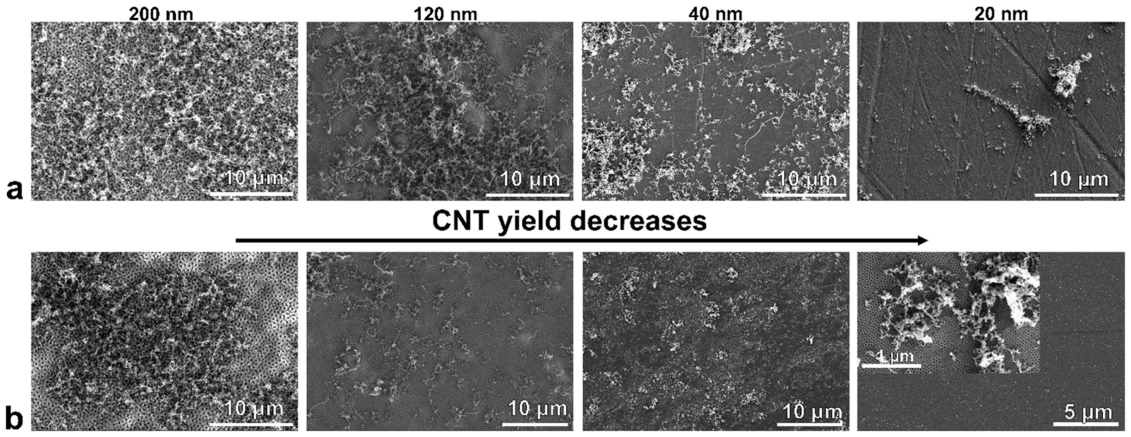

Figure 5. SEM images of the top surface (upper edge of cross sections shown in Figure 3) of AAO showing CNTs grown out of the nanopores (diameters labeled in the above images). The Ni MNWs shown here are either just (a) below the surface (45 μm) or (b) halfway down inside the nanopores (25 μm). Local high CNT yield shown inset (b) for 20 nm.

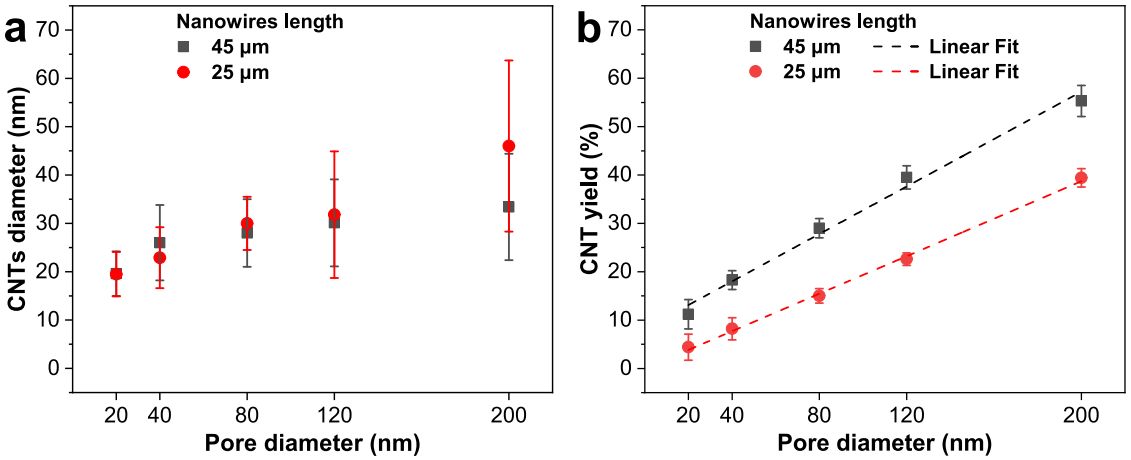

Figure 6. CNT mean diameter (a) and yield (b) depend on the AAO nanopore diameter and MNW length.

ratio of the D-to-G peaks (I_D/I_G, Figure 4a,b) serves as a measure of the degree of disorder of CNTs, with low values serving as a standard indicator of high CNT quality.[41] The I_D/I_G ratios somewhat increase with increasing nanopore diameter for 25 μm MNWs, whereas they fluctuate for 45 μm MNWs. The decreasedratio can be associated with both reducing CNT

https://doi.org/10.1021/acsanm.4c04782
ACS Appl. Nano Mater. 2024, 7, 24866−24874

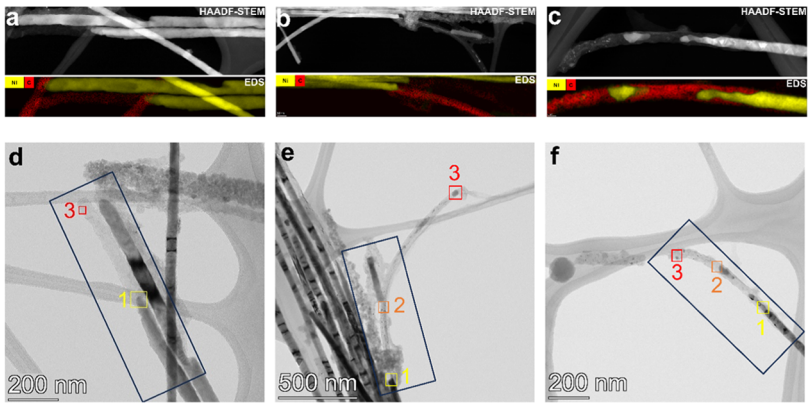

Figure 7. Images of CNT/MNW samples after release from the AAO template (40 nm nanopore sample). (a–c) Coupled HAADF–STEM–EDS images, where Ni is brighter/yellow and C is darker/red. (d–f) BF-TEM images for (d) bottom growth mode, (e) top-growth mode, and (f) mixed tip growth mode CNTs, where the numbers are in order of growth direction (from the CNT/MNW interface to the CNT tip) and boxes show the location of HAADF and EDS maps.

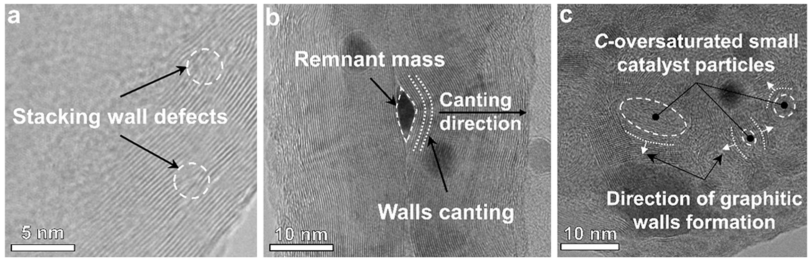

Figure 8. BF-TEM images of (a) region 3 from Figure 7d, (b) region 2 from Figure 7e, and (c) region 3 from Figure 7f.

density, thus diminishing the quantity of defective coiled CNTs contributing to the D peak and decreasing amorphous carbon (α-C). Although the difference is not very significant, the I_D/I_G ratios indicate that the most crystalline CNT samples were obtained when CVD growth occurred inside the templates (25 μm Ni MNW catalyst) with smaller diameter nanopores. Moreover, the I_D/I_G ratios for CNTs grown inside both (25 and 45 μm Ni MNW catalyst) 80 nm templates are close to 1, and 80 nm samples also demonstrated the best field emission, which is discussed later.

SEM images are shown in Figure 5. The CNTs were observed to grow out of the AAO nanopores with curling morphologies. The mean diameter of the CNTs was fairly constant at 30–40 nm for all diameters of catalyst MNWs when the tips of the MNWs were close to the top of the AAO surface (Figures 5a and 6a). However, when the catalyst MNWs were short, the CNTs grew deep (25 μm) inside the AAO nanopores, and the initial catalyst diameter appeared to have an effect. For 20 nm diameter MNW catalysts (and therefore also small nanopore diameters), the CNTs were of comparable diameter (Figures 5b and 6a). However, at larger diameters, it is likely that each catalyst MNW nucleated more than one CNT (Figure S2). The yield was estimated by the fraction of the surface containing CNTs, and it is summarized in Figure 6b.

The relatively high CNT nucleation density and growth activity are attributed to the unique properties of the feedstock. There are two primary roles of the feedstock in the growth observed. First, the feedstock promotes high carbon flux to the catalyst due to the complete dissociation of the hydrocarbon gases, including methane, which has high stability. Complete methane utilization requires temperatures above 800 °C.[13] However, complete utilization of the methane fraction in our feedstock is possible because free radicals are formed from the dissociation of relatively less stable unsaturated hydrocarbons (with much lower Gibbs free energies). These free radicals attack methane at our growth temperature (700 °C) to form carbon species. Second, the feedstock supports long catalyst lifetimes. Even though there is a high carbon flux to the catalyst, deactivation is suppressed due to the in situ generation of water in the vicinity of the catalyst via the reaction between hydrogen and CO.[45,46] In situ water generation has been verified experimentally and by thermodynamic calculations.[47] The formation of water close to the catalyst means coking can be suppressed as excess amorphous carbon formed can be removed via oxidation. This unique feature of FTS-GP can lead to an increase in the CNT nucleation density and catalyst lifetime. The low yield of CNTs from the embedded MNW in AAO can be improved with the optimization of many growth parameters.

The nucleation of CNTs from oversaturation of catalyst particles is similar to the classic catalysis mechanism described for thin films.[48] However, in the case of AAO with a short MNW, the feedstock gas supply must diffuse through the nanopore opening and down the nanopore to the Ni catalyst. As the AAO nanopore diameters decrease, diffusion may limit the ion species that can reach the Ni catalyst,[49] so the CNT yield decreases (Figure 6b). The maximum achieved CNT yield is 55% for 200 nm pore diameter and 45 μm MNW long and appears to be close to the average MNWs seed density (60–70% of pore density in Table 1).

TEM characterization was conducted to gain a better understanding of growth modes, specifically inside the AAO. Figures 7 and 8 show a difference in the bottom (Figure 7a,d),

https://doi.org/10.1021/acsanm.4c04782
ACS Appl. Nano Mater. 2024, 7, 24866–24874

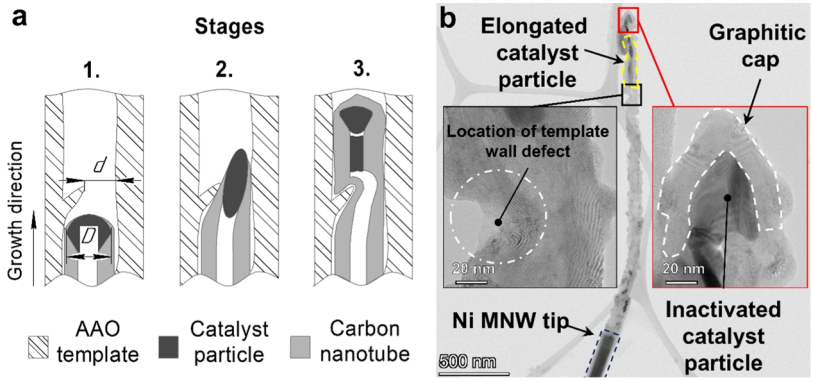

Figure 9. Suppression mechanism of top-growth mode by template pore wall defect: (a) schematic and (b) TEM image of such a mechanism (at stage 3) for MNW of 120 nm diameter.

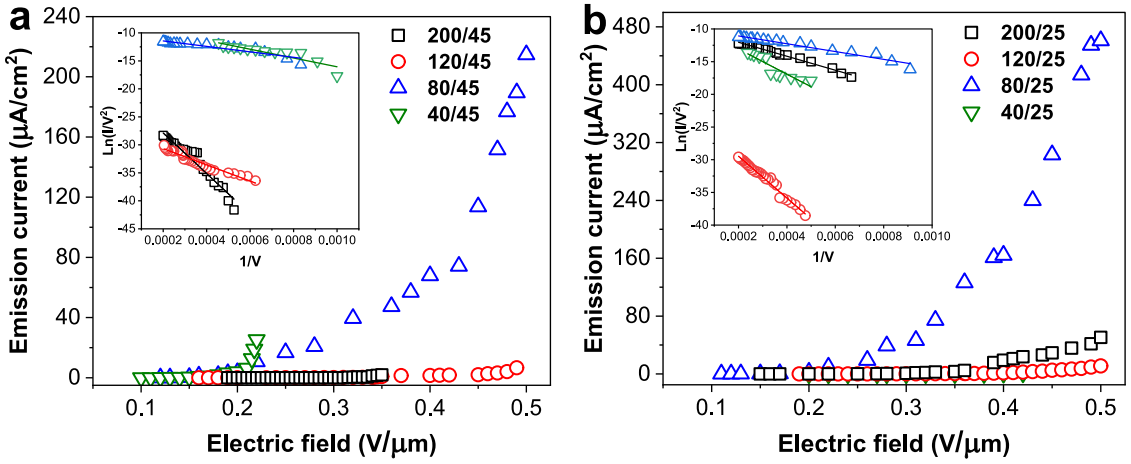

Figure 10. Field emission measurements of CNTs grown using (a) 45 and (b) 25 μm Ni MNW catalysts in AAO nanopores (diameters of emitters shown, where 20 nm did not yield field emission). Fowler–Nordheim plots are shown in the inset.

top (Figure 7b,e), and mixed (Figure 7c,f) CNT growth for a typical 40 nm nanopore diameter sample. High-angle annular dark field scanning TEM (HAADF-STEM) images show contrast when the atomic mass changes, so Ni is brighter than C in Figure 7a–c on top. X-ray energy dispersive spectroscopy (EDS) maps are element specific, and Ni is shown in yellow and C in Figure 7a–c below. Finally, several regions are marked in the bright-field TEM (BF-TEM) images of Figure 7d–f to show locations of the zoomed-in images of Figure 8, where the numbers go from "1" at the CNT/MNW interface, "2" along the CNT growth direction to "3" the tip of the CNT.

The bottom growth mechanism, where the pore diameter is small (20–40 nm) and gas diffusion is limited, mainly produces short CNTs (Figure 7a,d) with well-graphitized outer walls (Figure 8a) and inner areas filled with α-carbon, especially in the vicinity of the catalyst mass (Figure 7d, region 1). Some stacking wall defects are present (Figure 8a), which may be responsible for increasing the effective emission area.[50]

Top growth proceeds from a mass of Ni that has been lifted off of a MNW by the growing CNT. In contrast, the top-growth mode has a few distinctive features compared to the common one for thin films, where the moving catalyst is not restrained by any geometry and growth suppression is considered as least likely. Instead, suppression mechanisms of CNT growth inside an AAO template have been shown to include: precipitation of α-C onto the pore wall, thereby blocking the pore opening,[51,52] formation of multiwall nanotubes on the pore wall,[53] and inhibition of precursor gas diffusion during bottom growth mode.[53,54] Here, we report another distinct mechanism wherein Ni catalyst particles can become stuck at defects in the nanopore, which stops top growth (Figure 9). When a catalyst particle has a diameter D that is bigger than pore opening d at the defect site (Figure 9a, stage 1), then the particle is compressed by template walls and elongated, maintaining graphitic walls that follow the constrained pore geometry (Figure 9a, stage 2). After that, three cases may occur. First, the elongated particle may continue catalysis. Second, the elongated particle fragments due to friction or constraining forces of template walls[55] (Figures 7e,f and 9b). In this case, the separated particle may continue the catalysis of crystalline CNTs (Figure 7e, region 2) or amorphous carbon nanofibers (Figure 7f, region 2). Third, fragmentation may be accompanied by fast wall formation atop the catalyst, which leads to particle inactivation (Figures 9a, stage 3; 9b). Figure S3 shows more evidence of template pore wall defects and irregular MNWs and CNTs, supporting that the described mechanism is valid.

Moreover, the fragmentation phenomenon of the Ni catalyst mass can also be associated with a higher rate of CNT wall formation behind the catalyst. CNT wall compression can then cause deformation of the Ni mass stimulated by both elevated temperature and carbon oversaturation. The remnant mass remains stuck within the nanopore, which can cause wall defects, such as canting (Figure 8b). Another aspect to be

https://doi.org/10.1021/acsanm.4c04782
ACS Appl. Nano Mater. 2024, 7, 24866–24874

mentioned that prevailed in a curled CNT region (Figure 7e,f, regions 3) is small catalyst particles (5 and 20 nm) separated from the dominant one (Figure 8c). They can still act as a catalyst, but graphitic walls formed concentrically. In the case of multiple particles located in neighbors, they deactivate each other. Crystalline areas alternate with amorphous.

In spite of defects and growth suppression, this templated CNT growth process predominantly produces highly aligned crystalline CNTs regions. Also, Ni catalyst masses were not as likely to be stuck in larger diameter (80−200 nm) AAO nanopores, so bottom growth was more prominent. In fact, simultaneous growth of several CNTs from one MNW was observed with 200 nm MNWs (Figure S2).

While the primary focus of this work is the sustainable manufacture of Ni MNW catalyzed CNTs, one of our applications of interest is field emission. A low-power Keithley 2290-5 5 kV power source was used to measure the field emission characteristics of the samples, shown in Figure 10.

Values of 1−6 V/μm for the voltage required to reach a turn-on current of 10 μA/cm^2 were reported in the literature for similar samples[39,49,56,57] as well as freestanding CNT arrays[6,17] produced as possible field emitters. Our turn-on voltages to achieve the same current density were significantly lower, ranging from 0.2 to 0.5 V/μm. Moreover, our results are comparable to recent ones.[3,16] Xiao et al. reported threshold electric fields of 0.4 V/μm and emission currents of 70 μA/cm^2 at 0.65 V/μm.[3] Here, similar results were found with the 45 μm long MNWs, and even higher current densities were possible with 25 μm long MNWs, presumably due to the alignment of crystalline CNTs inside the nanopores before reaching the surface. Smaller diameter nanopores (20 and 40 nm) were shown above to yield shorter crystalline CNTs due to Ni catalyst masses being stuck inside the nanopores during the crystalline-producing top-growth mechanism. Larger diameter nanopores (120 and 200 nm) could produce several CNTs per nanowire, which appeared to limit emission, perhaps due to shielding. Therefore, 80 nm diameter nanopores appear to yield optimal performance in this initial study.

CNTs produced by sustainable manufacturing with a feedstock mixture of waste gases exhibited a field emission of 480 μA/cm^2 at 0.5 V/μm comparable to those formed from typical precursor gases,[58,59] showing promise for future gate electrode configurations. These results pave the way for future important applications, which can be realized with recycled waste resources.

4. CONCLUSIONS

CNTs were sustainably synthesized using industrial gaseous waste by thermal CVD inside nanopores of insulating membranes on predeposited nickel MNWs. This template-assisted thermal CVD manufacturing process is limited to temperatures below 800 °C due to structural transformation in anodic aluminum oxide templates. CNT yield increases with both pore diameter and the distance from the tip of MNWs to the template surface. A new CNT growth suppression mechanism was observed, namely, template pore wall defects, which can inhibit the motion of catalyst particles during top growth, especially in small pores. CNT defects result in wall canting, small particle inclusions with competitive catalytic activity, and, undesirable, particle inactivation. The highest field emission current (480 μA/cm^2 at 0.5 V/μm) was obtained with a 0.26 V/μm turn-on field from CNTs synthesized in templates with 80 nm pore diameters and 25 μm long Ni MNWs. This result is promising for future gate electrode applications.

ASSOCIATED CONTENT

Supporting Information

The Supporting Information is available free of charge at https://pubs.acs.org/doi/10.1021/acsanm.4c04782.

Roadmap of nickel magnetic nanowires deposition and carbon nanotube synthesis process (Figure S1); example of multiple CNTs nucleating from one pore for a sample of 200 nm pore diameter and 45 μm MNWs length (Figure S2); SEM of template cross-section and TEM images of template pore wall defects with corresponding irregular nanowires and carbon nanotubes grown atop them (Figure S3) (PDF)

AUTHOR INFORMATION

Corresponding Authors

Roman Kolisnyk − *Department of Electrical and Computer Engineering, University of Minnesota, Minneapolis, Minnesota 55455, United States;* orcid.org/0000-0002-0493-894X; Email: romanvaleriyovych@gmail.com

Bethanie J. H. Stadler − *Department of Electrical and Computer Engineering, University of Minnesota, Minneapolis, Minnesota 55455, United States*; Email: stadler@umn.edu

Authors

Morgen L. Smith − *Tim Taylor Department of Chemical Engineering, Kansas State University, Manhattan, Kansas 66506, United States;* orcid.org/0009-0003-1849-7051

Nicholas C. A. Seaton − *Characterization Facility, University of Minnesota, Minneapolis, Minnesota 55455, United States*

Michael L. Odlyzko − *Characterization Facility, University of Minnesota, Minneapolis, Minnesota 55455, United States*

Olha Masiuchok − *E.O. Paton Electric Welding Institute of NAS of Ukraine, Kyiv 03680, Ukraine;* orcid.org/0000-0002-3302-3079

Jeanne Riga − *Directed Energy Directorate, Air Force Research Laboratory, Albuquerque, New Mexico 87117, United States*

Placidus B. Amama − *Tim Taylor Department of Chemical Engineering, Kansas State University, Manhattan, Kansas 66506, United States;* orcid.org/0000-0001-9753-6044

Complete contact information is available at: https://pubs.acs.org/10.1021/acsanm.4c04782

Author Contributions

The manuscript was written through contributions of all authors. All authors have given approval to the final version of the manuscript.

Notes

The authors declare no competing financial interest.

ACKNOWLEDGMENTS

The authors gratefully acknowledge the support provided by the Air Force Office of Scientific Research (AFOSR) through Lab Task No. 21RDCOR008. Portions of this work were conducted in the Minnesota Nano Center and Characterization Facility, University of Minnesota, which are supported by the NSF through NNCI (Award Number ECCS-2025124) and MRSEC (Award Number DMR-2011401).

https://doi.org/10.1021/acsanm.4c04782
ACS Appl. Nano Mater. 2024, 7, 24866−24874

■ ABBREVIATIONS

CNTs, carbon nanotubes; MNWs, magnetic nanowires; AAO, anodic aluminum oxide; CVD, chemical vapor deposition; FTS, Fischer−Tropsch synthesis; α-C, amorphous carbon

■ REFERENCES

(1) Dresselhaus, M. S.; Dresselhaus, G.; Eklund, P. C. *Science of Fullerenes and Carbon Nanotubes*; Academic Press, 1996.

(2) Hekmat, F.; Sohrabi, B.; Rahmanifar, M. S.; Vaezi, M. R. Supercapacitive properties of coiled carbon nanotubes directly grown on nickel nanowires. *J. Mater. Chem. A* **2014**, *2* (41), 17446−17453.

(3) Xiao, D.; Du, H.; Sun, L.; Suo, X.; Wang, Y.; Zhang, Y.; Zhang, S.; Kuang, S.; Hu, F.; Tu, L.; et al. Boosting the electron beam transmittance of field emission cathode using a self-charging gate. *Nat. Commun.* **2024**, *15* (1), No. 764.

(4) Suresh, K. S.; Lahiri, I.; Kaur, G.; Kumar, V.; Bibhanshu, N. Influence of Surface Texture and Composition on Graphene Growth by Chemical Vapor Deposition on Cu−Ni Alloys for Field Emission Application. *ACS Appl. Nano Mater.* **2020**, *3* (10), 9804−9812.

(5) Devarapalli, R. R.; Kashid, R. V.; Deshmukh, A. B.; Sharma, P.; Das, M. R.; More, M. A.; Shelke, M. V. High efficiency electron field emission from protruded graphene oxide nanosheets supported on sharp silicon nanowires. *J. Mater. Chem. C* **2013**, *1* (33), 5040−5046.

(6) Lee, D. H.; Lee, J. A.; Lee, W. J.; Choi, D. S.; Lee, W. J.; Kim, S. O. Facile Fabrication and Field Emission of Metal-Particle-Decorated Vertical N-Doped Carbon Nanotube/Graphene Hybrid Films. *J. Mater. Chem. C* **2010**, *114* (49), 21184−21189.

(7) Li, J.; Ng, H. T.; Chen, H. Carbon Nanotubes and Nanowires for Biological Sensing. In *Protein Nanotechnology*; Vo-Dinh, T., Ed.; Methods in Molecular Biology; Humana Press: Totowa, NJ, 2005; Vol. *300*, pp 191−223.

(8) Tan, F.; Chen, H.; Yuan, R.; Zhang, X.; Chen, D. Co-Ni Basic Carbonate Nanowire/Carbon Nanotube Network with High Electrochemical Capacitive Performance via Electrochemical Conversion. *Front. Chem.* **2021**, *9*, No. 655025.

(9) Zhu, Y.; Li, X.; Xu, Y.; Wu, L.; Yu, A.; Lai, G.; Wei, Q.; Chi, H.; Jiang, N.; Fu, L.; et al. Intertwined Carbon Nanotubes and Ag Nanowires Constructed by Simple Solution Blending as Sensitive and Stable Chloramphenicol Sensors. *Sensors* **2021**, *21* (4), No. 1220.

(10) Correa-Duarte, M. A.; Salgueirino, V. Magnetic Properties of Nanowires Guided by Carbon Nanotubes. In *Nanowires Science and Technology*; Lupu, N., Ed.; InTech, 2010.

(11) Mamunya, Y.; Maruzhenko, O.; Kolisnyk, R.; Iurzhenko, M.; Pylypenko, A.; Masiuchok, O.; Godzierz, M.; Krivtsun, I.; Trzebicka, B.; Pruvost, S. Pyroresistive Properties of Composites Based on HDPE and Carbon Fillers. *Polymers* **2023**, *15* (9), No. 2105.

(12) Davis, B. F.; Yan, X.; Muralidharan, N.; Oakes, L.; Pint, C. L.; Maschmann, M. R. Electrically Conductive Hierarchical Carbon Nanotube Networks with Tunable Mechanical Response. *ACS Appl. Mater. Interfaces* **2016**, *8* (41), 28004−28011.

(13) Rao, R.; Pint, C. L.; Islam, A. E.; Weatherup, R. S.; Hofmann, S.; Meshot, E. R.; Wu, F.; Zhou, C.; Dee, N.; Amama, P. B.; et al. Carbon Nanotubes and Related Nanomaterials: Critical Advances and Challenges for Synthesis toward Mainstream Commercial Applications. *ACS Nano* **2018**, *12* (12), 11756−11784.

(14) Ren, Z. F.; Huang, Z. P.; et al. Synthesis of Large Arrays of Well-Aligned Carbon Nanotubes on Glass. *Science* **1998**, *282* (5391), 1105−1107.

(15) Han, J. S.; Lee, S. H.; Go, H.; Kim, S. J.; Noh, J. H.; Lee, C. J. High-Performance Cold Cathode X-ray Tubes Using a Carbon Nanotube Field Electron Emitter. *ACS Nano* **2022**, *16* (7), 10231−10241.

(16) Yi, C.; Wu, H.; Li, J.; Song, Y.; Song, Y.; Chen, X.; Ou-Yang, W. Crack-Assisted Field Emission Enhancement of Carbon Nanotube Films for Vacuum Electronics. *ACS Appl. Nano Mater.* **2019**, *2* (12), 7803−7809.

(17) Zhang, Y.; Tan, Y.; Wang, L.; Li, B.; Ke, Y.; Liao, M.; Xu, N.; Chen, J.; Deng, S. Electron Emission and Structure Stability of Carbon Nanotube Cold Cathode Driven by Millisecond Pulsed Voltage. *Vacuum* **2020**, *172*, No. 109071.

(18) Song, Y.; Li, J.; Wu, Q.; Yi, C.; Wu, H.; Chen, Z.; Ou-Yang, W. Study of film thickness effect on carbon nanotube based field emission devices. *J. Alloys Compd.* **2020**, *816*, No. 152648.

(19) De Jonge, N.; Bonard, J.-M. Carbon nanotube electron sources and applications. *Philos. Trans. R. Soc. London, Ser. A* **2004**, *362* (1823), 2239−2266.

(20) Dwivedi, N.; Dhand, C.; Carey, J. D.; Anderson, E. C.; Kumar, R.; Srivastava, A. K.; Malik, H. K.; Saifullah, M. S. M.; Kumar, S.; Lakshminarayanan, R.; et al. The rise of carbon materials for field emission. *J. Mater. Chem. C* **2021**, *9* (8), 2620−2659.

(21) De Heer, W. A.; Châtelain, A.; Ugarte, D. A Carbon Nanotube Field-Emission Electron Source. *Science* **1995**, *270* (5239), 1179−1180.

(22) Milne, W. I.; Teo, K. B. K.; Amaratunga, G. A. J.; Legagneux, P.; Gangloff, L.; Schnell, J.-P.; Semet, V.; Thien Binh, V.; Groening, O. Carbon nanotubes as field emission sources. *J. Mater. Chem.* **2004**, *14*, 933−943.

(23) Teo, K. B. K.; Minoux, E.; Hudanski, L.; Peauger, F.; Schnell, J.-P.; Gangloff, L.; Legagneux, P.; Dieumegard, D.; Amaratunga, G. A. J.; Milne, W. I. Microwave devices: Carbon nanotubes as cold cathodes. *Nature* **2005**, *437* (7061), No. 968.

(24) Kaur, G.; Dasgupta, A.; Korlam, S.; Modi, G.; Pulagara, N. V.; Lahiri, I. Carbon Nanotube-Based 2-Dimensional and 3-Dimensional Field Emitter Structures. *J. Electron. Mater.* **2021**, *50* (2), 483−490.

(25) Atthipalli, G.; Epur, R.; Kumta, P. N.; Allen, B. L.; Tang, Y.; Star, A.; Gray, J. L. The effect of temperature on the growth of carbon nanotubes on copper foil using a nickel thin film as catalyst. *Thin Solid Films* **2011**, *519* (16), 5371−5375.

(26) Hung, Y. J.; Huang, Y. J.; Chang, H. C.; Lee, K.-Y.; Lee, S.-L. Patterned growth of carbon nanotubes over vertically aligned silicon nanowire bundles for achieving uniform field emission. *Nanoscale Res. Lett.* **2014**, *9* (1), No. 540.

(27) Nilsson, L.; Groening, O.; Emmenegger, C.; Kuettel, O.; Schaller, E.; Schlapbach, L.; Kind, H.; Bonard, J.-M.; Kern, K. Scanning field emission from patterned carbon nanotube films. *Appl. Phys. Lett.* **2000**, *76* (15), 2071−2073.

(28) Che, G.; Lakshmi, B. B.; Martin, C. R.; Fisher, E. R.; Ruoff, R. S. Chemical Vapor Deposition Based Synthesis of Carbon Nanotubes and Nanofibers Using a Template method. *Chem. Mater.* **1998**, *10*, 260−267.

(29) Suh, J. S.; Lee, J. S. Highly ordered two-dimensional carbon nanotube arrays. *Appl. Phys. Lett.* **1999**, *75* (14), 2047−2049.

(30) Sui, Y. C.; Acosta, D. R.; González-León, J. A.; Bermúdez, A.; Feuchtwanger, J.; Cui, B. Z.; Flores, J. O.; Saniger, J. M. Structure, Thermal Stability, and Deformation of Multibranched Carbon Nanotubes Synthesized by CVD in the AAO Template. *J. Phys. Chem. B* **2001**, *105*, 1523−1527.

(31) Zamani Kouhpanji, M. R.; Ghoreyshi, A.; Visscher, P. B.; Stadler, B. J. H. Facile decoding of quantitative signatures from magnetic nanowire arrays. *Sci. Rep.* **2020**, *10* (1), No. 15482.

(32) Gilbert, D. A.; Murray, P. D.; De Rojas, J.; Dumas, R. K.; Davies, J. E.; Liu, K. Reconstructing phase-resolved hysteresis loops from first-order reversal curves. *Sci. Rep.* **2021**, *11* (1), No. 4018.

(33) Nemati, Z.; Kouhpanji, M. R. Z.; Zhou, F.; Das, R.; Makielski, K.; Um, J.; Phan, M.-H.; Muela, A.; Fdez-Gubieda, M. L.; et al. Isolation of cancer-derived exosomes using a variety of magnetic nanostructures: From Fe_3O_4 nanoparticles to Ni nanowires. *Nanomaterials* **2020**, *10* (9), No. 1662.

(34) Dennis, C. L.; Ivkov, R. Physics of heat generation using magnetic nanoparticles for hyperthermia. *Int. J. Hyperthermia* **2013**, *29* (8), 715−729.

(35) Chen, H.; Billington, D.; Riordan, E.; Blomgren, J.; Giblin, S. R.; Johansson, C.; Majetich, S. A. Tuning the dynamics in Fe_3O_4 nanoparticles for hyperthermia optimization. *Appl. Phys. Lett.* **2020**, *117* (7), No. 073702.

(36) Liu, J.; He, N.; Gui, Z.; Yan, Z.; He, J.; Li, X.; Jiang, R.; Yang, K.; Zhao, J.; Zeng, B. Multistage carbon nanotubes grown on foamed

https://doi.org/10.1021/acsanm.4c04782
ACS Appl. Nano Mater. 2024, 7, 24866−24874

nickel with organic solutions as multifunctional high performance electrodes. *Diamond Relat. Mater.* **2022**, *123*, No. 108807.
(37) Lv, S.; Li, Z.; Liao, J.; Zhang, Z.; Miao, W. Well-aligned NiSi/Si heterostructured nanowire arrays as field emitters. *J. Vac. Sci. Technol. B* **2015**, *33*, No. 02B101.
(38) Liu, R.-M.; Ting, J.-M.; Huang, J.-C. A.; Liu, C.-P. Growth of carbon nanotubes and nanowires using selected catalysts. *Thin Solid Films* **2002**, *420-421*, 145−150.
(39) Yen, J. H.; Leu, I. C.; Wu, M. T.; Lin, C. C.; Hon, M. H. Effect of nanowire catalyst for carbon nanotubes growth by ICP-CVD. *Diamond Relat. Mater.* **2005**, *14* (3), 841−845.
(40) Harpel, A.; Um, J.; Dave, A.; Zhang, Y.; Mahjabeen, N.; Chen, Y.; Henderson, R.; Franklin, R.; Stadler, B. J. H. Vertically Integrated Nanowires on Si Wafers and Into Circuits. *IEEE Trans. Magn.* **2023**, *59* (3), No. 3200505.
(41) Li, Z.; Deng, L.; Kinloch, I. A.; Young, R. J. Raman spectroscopy of carbon materials and their composites: Graphene, nanotubes and fibres. *Prog. Mater. Sci.* **2023**, *135*, No. 101089.
(42) Nemanich, R. J.; Solin, S. A. First- and second-order Raman scattering from finite-size crystals of graphite. *Phys. Rev. B* **1979**, *20*, 392−401.
(43) Heise, H. M.; Kuckuk, R.; Ojha, A.; Srivastava, A.; Srivastava, V.; Asthana, B. Characterisation of carbonaceous materials using Raman spectroscopy: a comparison of carbon nanotube filters, single- and multi-walled nanotubes, graphitised porous carbon and graphite. *J. Raman Spectrosc.* **2009**, *40* (3), 344−353.
(44) Merlen, A.; Buijnsters, J. G.; Pardanaud, C. A Guide to and Review of the Use of Multiwavelength Raman Spectroscopy for Characterizing Defective Aromatic Carbon Solids: from Graphene to Amorphous Carbons. *Coatings* **2017**, *7*, No. 153.
(45) Almkhelfe, H.; Carpena-Núñez, J.; Back, T. C.; Amama, P. B. Gaseous product mixture from Fischer−Tropsch synthesis as an efficient carbon feedstock for low temperature CVD growth of carbon nanotube carpets. *Nanoscale* **2016**, *8* (27), 13476−13487.
(46) Almkhelfe, H.; Li, X.; Rao, R.; Amama, P. B. Catalytic CVD growth of millimeter-tall single-wall carbon nanotube carpets using industrial gaseous waste as a feedstock. *Carbon* **2017**, *116*, 181−190.
(47) Everhart, B. M.; Almkhelfe, H.; Li, X.; Wales, M.; Nikolaev, P.; Rao, R.; Maruyama, B.; Amama, P. B. Efficient Growth of Carbon Nanotube Carpets Enabled by In Situ Generation of Water. *Ind. Eng. Chem. Res.* **2020**, *59* (19), 9095−9104.
(48) Sato, H.; Hori, Y.; Hata, K.; Seko, K.; Nakahara, H.; Saito, Y. Effect of catalyst oxidation on the growth of carbon nanotubes by thermal chemical vapor deposition. *J. Appl. Phys.* **2006**, *100* (10), No. 104321.
(49) Yen, J.-H.; Leu, I.-C.; Wu, M.-T.; Lin, C.-C.; Hon, M.-H. Growth characteristics of carbon nanotube arrays synthesized by ICP-CVD using anodic aluminum oxide on silicon as a nanotemplate. *Chem. Vap. Deposition* **2005**, *11* (4), 219−225.
(50) Saito, Y.; Uemura, S. Field emission from carbon nanotubes and its application to electron source. *Carbon* **2000**, *38*, 169−182.
(51) Lin, C.-C.; Pan, F.-M.; Chang, K.-C.; Kuo, C.-W.; Kuo, C.-T. Mechanistic study of cobalt catalyzed growth of carbon nanofibers in a confined space by plasma-assisted chemical vapor deposition. *Diamond Relat. Mater.* **2009**, *18* (10), 1301−1305.
(52) Jeong, S.-H.; Hwang, H.-Y.; Hwang, S.-K.; Lee, K.-H. Carbon Nanotubes Based on Anodic Aluminum Oxide Nano-Template. *Carbon* **2004**, *42* (10), 2073−2080.
(53) Lee, J. S.; Gu, G. H.; Kim, H.; Jeong, K. S.; Bae, J.; Suh, J. S. Growth of Carbon Nanotubes on Anodic Aluminum Oxide Templates: Fabrication of a Tube-in-Tube and Linearly Joined Tube. *Chem. Mater.* **2001**, *13* (7), 2387−2391.
(54) Chen, P.-L.; Chang, J.-K.; Kuo, C.-T.; Pan, F.-M. Anodic aluminum oxide template assisted growth of vertically aligned carbon nanotube arrays by ECR-CVD. *Diamond Relat. Mater.* **2004**, *13* (11−12), 1949−1953.
(55) Deck, C. P.; Vecchio, K. Growth mechanism of vapor phase CVD-grown multi-walled carbon nanotubes. *Carbon* **2005**, *43* (12), 2608−2617.
(56) Wu, Q. B.; Ren, S.; Deng, S. Z.; Chen, J.; She, J. C.; Xu, N. S. Template-based synthesis of carbon nanofibres and their field emission characteristics. *Surf. Interface Anal.* **2004**, *36*, 493−496.
(57) Suh, J. S.; Jeong, K. S.; Lee, J. S.; Han, I. Study of the field-screening effect of highly ordered carbon nanotube arrays. *Appl. Phys. Lett.* **2002**, *80* (13), 2392−2394.
(58) Davydov, D. N.; Sattari, P. A.; AlMawlawi, D.; Osika, A.; Haslett, T. L.; Moskovits, M. Field Emitters Based on Porous Aluminum Oxide Templates. *J. Appl. Phys.* **1999**, *86*, 3983−3987.
(59) Gao, H.; Mu, C.; Wang, F.; Xu, D.; Wu, K.; Xie, Y.; Liu, S.; Wang, E.; Xu, J.; Yu, D. Field Emission of Large-Area and Graphitized Carbon Nanotube Array on Anodic Aluminum Oxide Template. *J. Appl. Phys.* **2003**, *93*, 5602−5605.

https://doi.org/10.1021/acsanm.4c04782
ACS Appl. Nano Mater. 2024, 7, 24866−24874